

RESEARCH ARTICLE | OCTOBER 04 2023

Presence of a chiral soliton lattice in the chiral helimagnet MnTa_3S_6

Y. Miyagi; J. Jiang ; K. Ohishi ; Y. Kawamura ; J. Suzuki; D. R. Alshalawi ; J. Campo ; Y. Kousaka  ; Y. Togawa 



APL Mater. 11, 101105 (2023)
<https://doi.org/10.1063/5.0171790>



CrossMark

AIP Advances

Why Publish With Us?

-  **25 DAYS**
average time to 1st decision
-  **740+ DOWNLOADS**
average per article
-  **INCLUSIVE**
scope



[Learn More](#)



Presence of a chiral soliton lattice in the chiral helimagnet MnTa_3S_6

Cite as: APL Mater. 11, 101105 (2023); doi: 10.1063/5.0171790
Submitted: 10 August 2023 • Accepted: 18 September 2023 •
Published Online: 4 October 2023



Y. Miyagi,¹ J. Jiang,¹  K. Ohishi,²  Y. Kawamura,²  J. Suzuki,² D. R. Alshalawi,^{2,3,4}  J. Campo,⁵ 
Y. Kousaka,^{1,a)}  and Y. Togawa¹ 

AFFILIATIONS

¹Department of Physics and Electronics, Osaka Metropolitan University, Sakai, Osaka 599-8531, Japan

²Neutron Science and Technology Center, Comprehensive Research Organization for Science and Society (CROSS), Tokai, Ibaraki 319-1106, Japan

³Institute of Applied Magnetism, UCM-ADIF-CSIC, Las Rozas 28230, Spain

⁴Department of Materials Physics, Complutense University of Madrid, Madrid 28040, Spain

⁵Aragón Nanoscience and Materials Institute (CSIC - University of Zaragoza) and Condensed Matter Physics Department, C/Pedro Cerbuna 12, 50009 Zaragoza, Spain

^{a)}Author to whom correspondence should be addressed: koyu@omu.ac.jp

ABSTRACT

Chiral helimagnetism was investigated in transition-metal intercalated dichalcogenide single crystals of MnTa_3S_6 . Small-angle neutron scattering (SANS) experiments revealed the presence of harmonic chiral helimagnetic order, which was successfully detected as a pair of satellite peaks in the SANS pattern. The magnetization data are also supportive of the presence of chiral soliton lattice (CSL) phase in MnTa_3S_6 . The observed features are summarized in the phase diagram of MnTa_3S_6 , which is in strong contrast with that observed in other dichalcogenides such as CrNb_3S_6 and CrTa_3S_6 . The presence of the remanent state provides tunable capability of the number of chiral solitons at zero magnetic field in the CSL system, which may be useful for memory device applications.

© 2023 Author(s). All article content, except where otherwise noted, is licensed under a Creative Commons Attribution (CC BY) license (<http://creativecommons.org/licenses/by/4.0/>). <https://doi.org/10.1063/5.0171790>

I. INTRODUCTION

Chiral helimagnets generate chiral magnetic structures because of a competition between antisymmetric Dzyaloshinskii–Moriya (DM) interaction^{1,2} and symmetric Heisenberg exchange interaction. A chiral helimagnetic structure (CHM) appears at zero magnetic field,^{3,4} while a nontrivial helicoidal transformation from the CHM to a chiral soliton lattice (CSL)^{5–16} occurs in the presence of magnetic fields, as schematically drawn in Fig. 1(a). Chiral magnetic vortices called magnetic skyrmions also appear in some chiral helimagnets.^{17–20}

The CSL is a tunable superlattice of magnetic moments with robust phase coherence,¹⁰ and thus, topological and collective responses appear in the CSL system. For instance, the CSL exhibits multivalued MR effect,^{21,22} nonreciprocal electrical transport,²³ and collective elementary excitation in a sub-terahertz frequency regime.²⁴ Moreover, the magnetic Goos Hanchen effect

was demonstrated in uniaxial helimagnets with CSL.²⁵ Such unique features may open up a novel route of spintronic, magnonic, and 6G communication device applications using the CSL.^{26–28}

Transition-metal intercalated dichalcogenides (TMD) $M'M_3S_6$ ($M' = 3d$ transition metal, $M = \text{Nb}$ or Ta) have attracted attention since the observation of the CHM and CSL in CrNb_3S_6 . It forms a chiral monoaxial crystal structure with a space group $P6_322$,^{29–31} as shown in Fig. 1(b). In CrNb_3S_6 , the CHM formation was detected by small-angle neutron scattering (SANS) experiments,⁴ while the CSL formation was directly observed by Lorentz microscopy.¹⁰

Note that the CHM period at zero magnetic field $L(0)$ is given as $2\pi(J/D)a_0$, where J is the symmetric exchange interaction, D is that of DM interaction, and a_0 is the size of the unit cell along the c-axis. A typical period of the CHM is several tens of nm because D is much smaller than that of J . The corresponding wave number of the harmonic CHM is typically 0.1 nm^{-1} or less. Thus, neutron scattering experiments should be performed with a

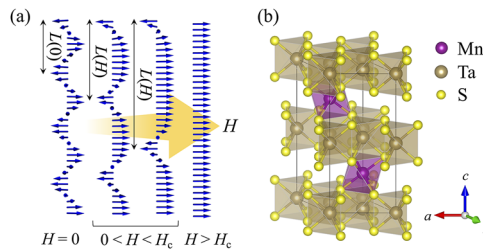


FIG. 1. (a) Evolution of chiral magnetic structures when increasing the magnetic field perpendicular to the c-axis. The chiral helimagnetic order (CHM) transforms into a forced ferromagnetic state (FFM) via a chiral soliton lattice (CSL). (b) Crystal structure of MnTa_3S_6 .

spatial resolution in Q enough to probe magnetic satellite peaks.^{3,4} The magnetic structures of TMDs were sometimes misinterpreted as ferromagnetic (FM) because of the difficulty to discern these magnetic satellite peaks by using SANS experiments.

Moreover, it is important to grow high-quality TMD crystals that host the CHM and CSL because a small amount of defects of intercalated transition metals stabilizes the FM ordering rather than the CHM and CSL formation.³² Indeed, MnNb_3S_6 and CrTa_3S_6 were first reported to exhibit the ferromagnetic order.^{29,31,33–36} However, in fact, high quality single crystals of these compounds were reexamined and found to form the CHM and CSL.^{37–42} The values of a critical temperature T_c , a critical magnetic field H_c , $L(0)$, and J/D in the chiral helimagnetic TMDs are summarized in Table I.

It was reported that MnTa_3S_6 , which forms the same crystal structure as CrNb_3S_6 , showed ferromagnetism with a Curie temperature T_c of 70 K with the magnetic easy axis lying in the hexagonal basal plane.^{29,31,33,35,36,43,44} When an external magnetic field H was applied in the direction perpendicular to the c-axis, the magnetization showed a small anomaly at 35 K. The magnetization curve at 2 K presented a tiny hysteresis loop near the saturation field.⁴³ Nanoflake samples exhibited a topological Hall effect in H parallel to the c-axis.⁴⁴ However, no studies were reported about the presence of the CHM and CSL formation in MnTa_3S_6 single crystals, which constitute the main focus of this paper.

We investigated the magnetic structures of MnTa_3S_6 using SANS and magnetization experiments with high-quality single crystals. The SANS experiments detected magnetic satellite peaks along the c-axis, indicating the CHM with the period of 86 nm. The magnetization measurements, via a zero-field cooling process, also revealed the CSL formation as observed in other TMDs such as CrNb_3S_6 and CrTa_3S_6 . The hysteresis in the magnetization curves makes a

TABLE I. A list of T_c , H_c , the CHM period $L(0)$, and J/D for chiral helimagnetic TMDs. The values of the Cr-intercalated TMDs are taken from the literature for CrNb_3S_6 ^{4,32,37} and CrTa_3S_6 .^{39–42} The values of MnTa_3S_6 are deduced from this work.

	T_c (K)	H_c (T)	$L(0)$ (nm)	D/J
CrNb_3S_6	133	0.2	48	0.16
CrTa_3S_6	150	1.7	22	0.35
MnTa_3S_6	35	0.7	86	0.09

magnetic phase diagram complicated as compared to other TMDs that exhibit chiral helimagnetism. However, the presence of the remanent state may open up the development of memory device applications using chiral solitons as multiple information bits.

II. EXPERIMENTAL METHODS

Single crystals of MnTa_3S_6 were grown by means of chemical vapor transport (CVT), which is the same method as that used in the crystal growth of CrNb_3S_6 .^{4,37} The polycrystalline powders were synthesized as a precursor for the crystal growth by using the gas phase method with a mixture of Mn, Ta, and S in the molar ratio of $x_{\text{nominal}}:3:6$. The CVT growth was performed with an evacuated silica tube in a temperature gradient using iodine as a transport agent. The precursor was placed at one end of the silica tube and then heated in the electric tube furnace under the fixed temperature gradient from 1100 to 1000 °C for ten days. The single crystals were grown at the other end of the silica tube. The obtained crystals have the shape of a hexagonal plane of 1 to 4 mm in diameter and of 0.1 to 0.5 mm in thickness.

Note that an emergence of chiral helimagnetism in the grown TMD crystals is very sensitive to x_{nominal} of the polycrystalline precursor. It was reported that in the case of CrNb_3S_6 ³² and CrTa_3S_6 ,⁴² the amount of Cr in the grown crystals was not necessarily fixed to a stoichiometric composition (the unity). Importantly, it was analyzed to be smaller than x_{nominal} of the polycrystalline precursors used in the CVT growth. As a consequence, x_{nominal} was tuned to be a value larger than the unity in order to obtain single crystals without Cr defects that host the CHM and CSL. These results indicate the importance of an optimization of the crystal growth condition in terms of x_{nominal} . Indeed, in the crystal growth of MnTa_3S_6 , ferromagnetic single crystals were obtained from the precursors with the stoichiometric composition ($x_{\text{nominal}} = 1$).^{43,44}

To examine the magnetic structure, zero-field SANS experiments were performed at BL15 (TAIKAN)⁴⁵ at the Material and Life Science Experimental Facility (MLF) in J-PARC, Japan. The crystal was aligned with the $[001]^*$ direction parallel to the scattering vector; the incident neutron beam with a wavelength from 0.8 to 1.5 nm was directed along the $[1\bar{2}0]^*$ direction. Scans in ω were performed to detect and maximize the magnetic satellite peak intensity at the (00δ) and $(00\bar{\delta})$ direction. To obtain the magnetic scattering signals, large background intensity due to the incident neutron beam at low wave vector Q region was subtracted from the SANS patterns at each temperature T .

The magnetization of the obtained single crystal was collected with H applied in the direction perpendicular to the c-axis using a SQUID magnetometer (Quantum Design MPMS 3). The magnetization was measured as a function of T in the zero-field cooling (ZFC) and field-cooling (FC) processes. The magnetization was also examined in cycling H at different temperatures.

III. RESULTS

A. Crystal optimization

Single crystals were grown from the precursors with x_{nominal} from 1.00 to 1.35 for the x_{nominal} optimization. As a result, the single crystal with x_{nominal} fixed to be 1.14 exhibited downward convex

behavior of the magnetization, which could be regarded as a manifestation of the CSL formation as discussed in other TMDs hosting the CHM and CSL,^{37,40–42} while the crystals from other x_{nominal} values showed ferromagnetic behavior.

B. Small-angle neutron scattering (SANS)

The SANS experiments revealed the presence of the CHM along the caxis at zero H , as shown in Fig. 2(a), which shows the Q -scan profiles along the caxis at different temperatures. Here, the SANS patterns were converted to the Q profiles along the $[001]^*$ direction integrating in the signal over a 20° angular sector.

As shown in Fig. 2(b), a pair of the magnetic satellite peaks was clearly observed along the $[001]^*$ direction, which is parallel to Q_x , in the SANS pattern at 2 K after the background subtraction using the paramagnetic data at 100 K. As shown in Fig. 2(c), the magnetic peak was clearly observed at 0.073 nm^{-1} in the Q -scan profiles along the $[001]^*$ direction after a background subtraction of the incident neutron beam intensity. The peak position in Q -space produces a period of 86 nm in real space. The magnetic period in MnTa_3S_6 is longer than those in CrNb_3S_6 ^{4,10} and in CrTa_3S_6 .³⁹ Moreover, additional SANS peaks were not detected at higher harmonic positions. Therefore, these magnetic satellite peaks are the first real evidence of the presence of a CHM phase stabilized by the DM interaction in MnTa_3S_6 crystals.

Figure 2(d) shows that the Q -position (the period of the helix) and intensity of the magnetic satellite peaks do not depend on T below a critical temperature T_c at 35 K, determined by magnetization measurements discussed later. Such a tendency was found even in the Q profile at 37 K, which is slightly higher than T_c . The intensity drastically decreases with further increasing T and vanishes in the T regime for the paramagnetic phase as seen in the SANS data at 75 and 100 K in Fig. 2(a).

C. Magnetic measurements

The T dependence of the magnetization at fixed magnetic field H (0.01 T) in MnTa_3S_6 single crystals is shown in Fig. 3(a). The Curie–Weiss temperature θ_{CW} , determined by fitting the inverse susceptibility in the paramagnetic region to the Curie–Weiss law, is 67 K. With decreasing T , the magnetization increases at around 100 K. After a rapid increase in the magnetization below θ_{CW} , it sharply drops at 35 K. Here, a critical temperature T_c is defined at the peak position of the magnetization,^{4,9} as shown in Fig. 3(a). With increasing H strength, the magnetization peak shifts toward lower T , as observed in Fig. 3(b). Such behavior of the magnetization is consistent with those observed in CrNb_3S_6 ^{32,37,38} and CrTa_3S_6 .^{40–42} In this respect, these results support the formation of CHM and CSL in the present MnTa_3S_6 crystal with the H oriented perpendicular to the caxis.

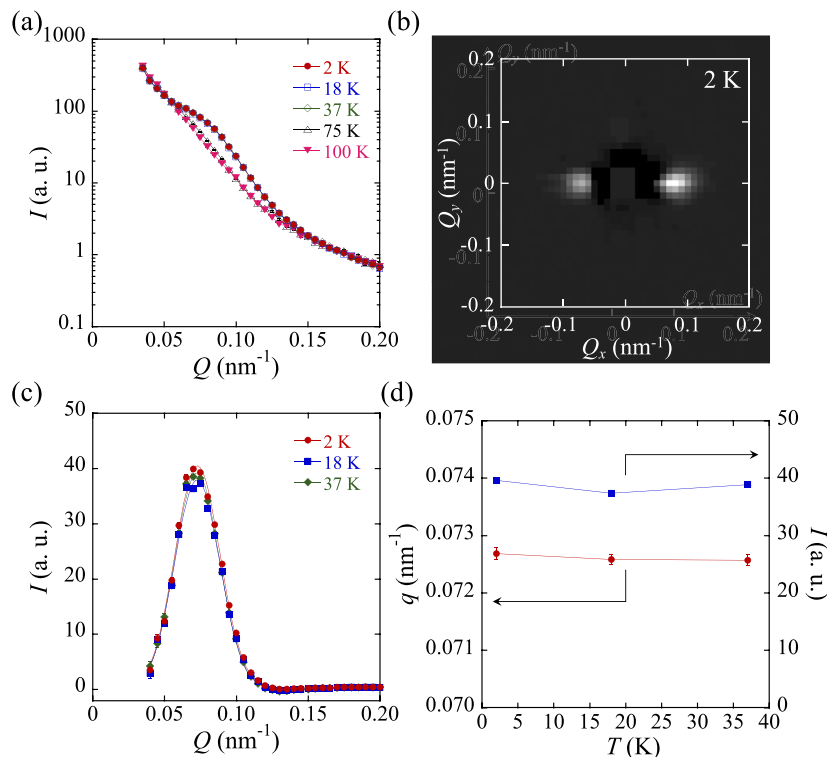


FIG. 2. (a) The SANS profiles of the MnTa_3S_6 single crystal obtained by Q scan along the caxis measured at different temperatures. (b) A map of the magnetic SANS intensity collected at 2 K. The paramagnetic signal at 100 K was subtracted as a background signal from the original data. (c) The magnetic profiles along the caxis, processed by a subtraction of the incident neutron beam intensity as a background signal. (d) The temperature dependence of the magnetic satellite peak position and peak intensity.

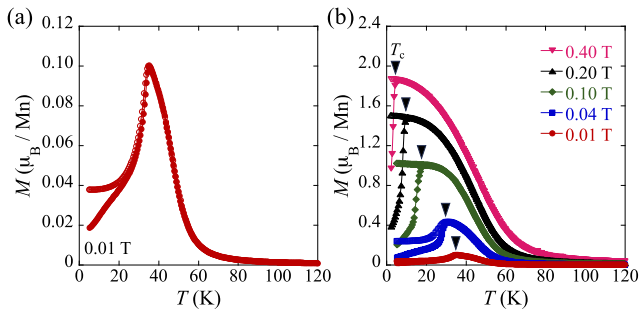


FIG. 3. Temperature dependence of the magnetization in the MnTa₃S₆ single crystal measured with H perpendicular to the caxis collected at 0.01 T (a) and higher H s up to 0.40 T (b). Closed and open marks denote the magnetization data collected in the zero-field cooling (ZFC) and field cooling (FC) procedures, respectively.

Note that a deviation of the magnetization between the ZFC and FC procedures becomes evident in the T regime below T_c . Figure 3(b) shows that in the ZFC process, the magnetization peak survives until temperatures go down to 2 K, which corresponds to the lowest T measured in this study, while it disappears for H s at around 0.1 T in the FC process.

To examine the CSL formation in MnTa₃S₆, isothermal magnetization vs field curves were measured below T_c . Note that the initial state was prepared via the ZFC process in every measurement in Fig. 4. Downward convex behavior of the magnetization curves was observed in the H increase process at temperatures ranging from 2 to 33 K, which is consistent with the magnetization behavior expected for the CSL formation as established in CrNb₃S₆^{37,38} and CrTa₃S₆.^{40,41} This observation indicates that the CSL formation occurs in the present MnTa₃S₆ crystal.

Hysteresis behavior appears in the decreasing H process ($0 \leq H_{+max} \rightarrow 0$). Here, we defined a critical magnetic field H_c as the irreversibility onset of the magnetization. The H_c value decreases with increasing T , as seen in Figs. 4(b) and 4(d).

In addition, a sharp drop of the magnetization was found at small H s when decreasing the H in the low T regime, as indicated by H^- in Fig. 4(b). It could be related with the penetration of chiral solitons into the system because of the disappearance of the surface barrier as discussed in CrNb₃S₆¹¹ and CrTa₃S₆.⁴² As a result, a distorted CSL with many dislocations should be formed at H^- as experimentally observed in CrNb₃S₆.^{46–48} The H^- position shifts toward smaller H s with increasing T , and eventually, it disappears at 15 K.

Alternatively, the magnetization gradually decreases in the decreasing H process in the high T regime, as seen in Fig. 4(d). The magnetization curves for increasing and decreasing the H merge, providing H^* as the end point of the hysteresis. Namely, the reversibility of the magnetization is recovered below H^* . The behavior of H^* with respect to T shows that H^* reaches the maximum value at 25 K and decreases at higher T because of the suppression of H_c . In this regime, the net magnetization vanishes on average at zero H , which is a strong indication of the presence of the ideal CHM without any dislocation above 15 K.^{46,47}

Moreover, a residual magnetization remains at zero H in the low T regime as seen in the H decreasing curves in Fig. 4(a). Such a spontaneous magnetization almost disappears at 15 K.

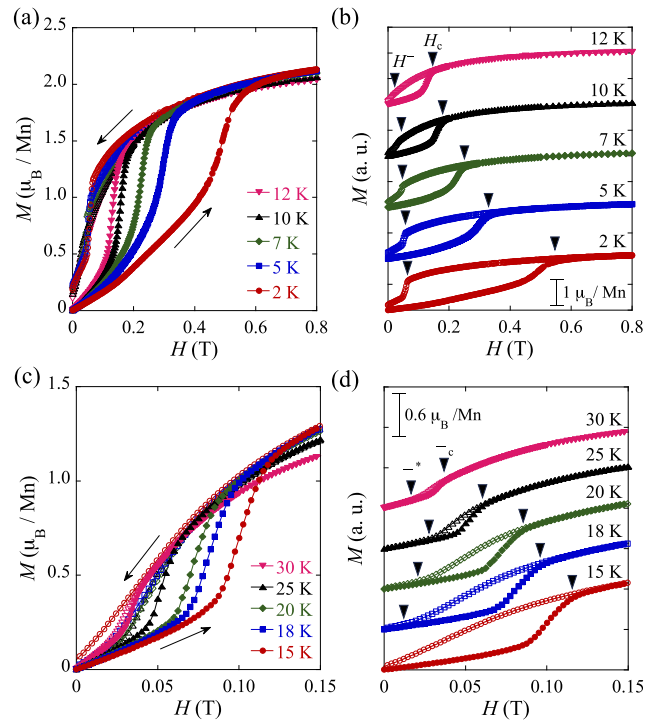


FIG. 4. Magnetic field dependence of the magnetization in the MnTa₃S₆ single crystal with H applied in the direction perpendicular to the caxis. The data were collected at temperatures from 2 to 12 K (a) and (b) and from 15 to 30 K (c) and (d). Closed and open marks denote the magnetization data collected in the H increase and decrease processes, respectively.

A hysteresis full loop of the magnetization was measured below 15 K at 2 and 7 K as shown in Fig. 5. It shows that when decreasing, $0 \leq H_{+max} \rightarrow 0$ (increasing, $0 \geq H_{-max} \rightarrow 0$), the H to zero after being saturated at positive (negative) large values, H_{+max} (H_{-max}), and

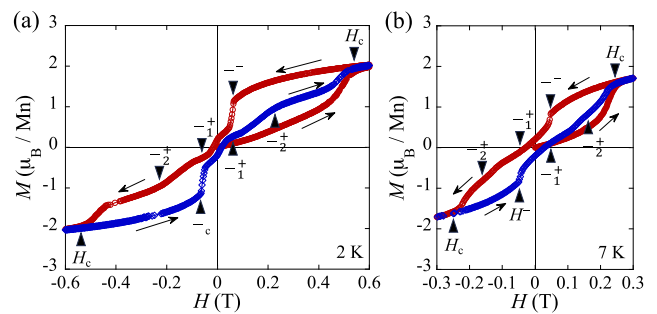


FIG. 5. A hysteresis loop of the magnetization in the MnTa₃S₆ single crystal at 2 K (a) and 7 K (b) with H applied in the direction perpendicular to the caxis. The data, collected between 1 and -1 T, were zoomed to see the magnetization curves below H_c . Closed red circles denote the magnetization curve when increasing the H from zero H with the initial state prepared via the ZFC process. Open red circles and blue diamonds denote the magnetization curves collected when decreasing and increasing H processes, respectively.

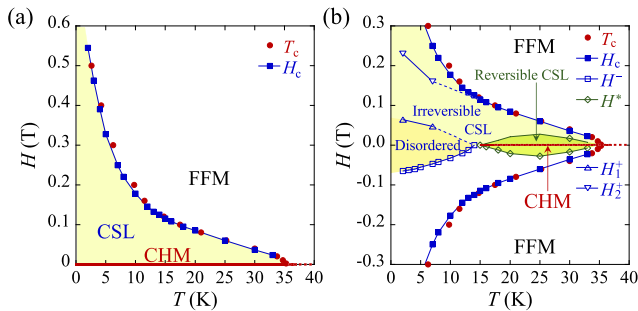


FIG. 6. Magnetic phase diagram of the MnTa₃S₆ single crystal, determined by the magnetization curves. The data were collected with the initial state in the ZFC process (a) and taken by hysteresis loops with the H sweep from -1 to 1 T (b).

passing through H^- , upward convex behavior of the magnetization appears in the vicinity of zero H .

This feature could be explained due to a reorientation process of the magnetic moments via their collective rotation so as to recover the CHM. Then, downward convex behavior, which could be associated with the CSL formation, starts to appear above a given H . Such behavior was observed repeatedly in the low T regime as indicated by the onsets of H_1^+ and H_2^+ in Figs. 5(a) and 5(b).

The experimental data obtained in the present MnTa₃S₆ crystal are summarized in the phase diagram depicted in Fig. 6. A simple phase diagram is obtained when measuring using the ZFC protocol, as shown in Fig. 6(a). The CHM exists at zero H below T_c as confirmed in the SANS data, and it transforms into the CSL with the increase in H applied perpendicularly to the caxis. T_c and H_c coincide with each other, providing the phase boundary between the CSL and forced ferromagnetic (FFM) state. Interestingly, the boundary line expands toward higher H s below 15 K. An extrapolation of the H_c boundary line below 15 K gives 0.7 T at 0 K, while an extrapolation of the boundary in the high temperature regime provides 0.2 T. The origin of this feature remains to be clarified although similar behavior was reported in MnNb₃S₆.⁴⁹

Figure 6(b) shows the phase diagram when decreasing the H from the saturated FFM state to zero ($0 \leq H_{+\max} \rightarrow 0$). The hysteresis survives far below H_c , indicating an expansion of the FFM region. The remanent state appears at zero H below 15 K. This magnetic state should correspond to the distorted CHM since it is generated from the disordered CSL with soliton defects that is formed at H^- ^{46–48} and leaves the residual magnetization even at zero H . Moreover, the CSL region is likely to be divided into the low and high H regime below 15 K as recognized by the magnetization anomaly (given by H_1^+ and H_2^+) in the full loop of the magnetization.

On the other hand, a doom-shaped region, enclosed by H^* , appears in the high T regime between 15 K and T_c . Here, the CHM appears at zero H and transforms into the CSL when increasing the H . Nonlinearity in the CSL develops slowly in this regime^{26,27} although irreversible behavior of the magnetization becomes evident above H^* .

The magnetization curve at 15 K is quite interesting since the gradual reduction in the magnetization continues down to zero H with decreasing H ($0 \leq H_{+\max} \rightarrow 0$) and is followed by the CSL formation when increasing again H . Further investigations are required

to reveal such a continuous magnetization process⁵⁰ observed at 15 K in Fig. 4(d).

In summary, our experiments show unambiguously that chiral helimagnetism is present in MnTa₃S₆ single crystals when they are carefully grown. The CHM phase was directly observed as a pair of satellite peaks in the SANS experiments. The magnetization measurements support the presence of CHM and CSL phases as well. However, the irreversible behavior observed in the magnetization curves in MnTa₃S₆ needs to be still clarified. We determined the phase diagram of MnTa₃S₆, which is dependent on the initial state at zero H in contrast with those observed in other TMDs such as CrNb₃S₆ and CrTa₃S₆. The material parameters of TMDs hosting the CHM and CSL are summarized in Table I. Detailed analyses using SANS under applied H s, resonant X-ray magnetic scattering,⁵¹ and Lorentz microscopy^{10,46,48} are required for further understanding of the nature of different magnetic states observed in the proposed magnetic phase diagram.

For instance, the temperature dependence of the magnetic satellite intensity should be examined in detail using the SANS technique, which will allow an evaluation of the T evolution of the DM interaction constant. Furthermore, the presence of the remanent state in MnTa₃S₆ is worth investigation since it gives coercivity to chiral solitons in the CSL system. Namely, tunable capability of the soliton number at zero H emerges in TMDs, which may open up the possibility to develop memory bits using the CSL system.

ACKNOWLEDGMENTS

This work was supported by JSPS KAKENHI Grant Nos. 17H02815, 19H05822, 19H05826, 19KK0070, 21H01032, 23H01870, and 23H00091. Grant No. PID2022-138492NB-I00-XM4 funded by MCIN/AEI/10.13039/501100011033, OTR02223-SpINS from CSIC/MCIN, and DGA/M4 from Diputación General de Aragón (Spain) are also acknowledged. The SANS experiments at the MLF of the J-PARC were performed under user programs (Proposal Nos. 2020C0001, 2021B0265, 2022B0232, and 2023A0167).

AUTHOR DECLARATIONS

Conflict of Interest

The authors have no conflicts to disclose.

Author Contributions

Y. Miyagi: Investigation (equal); **J. Jiang:** Data curation (supporting); Investigation (supporting); **K. Ohishi:** Data curation (equal); Investigation (equal); **Y. Kawamura:** Data curation (supporting); Investigation (supporting); **J. Suzuki:** Data curation (supporting); Investigation (supporting); **D. R. Alshalawi:** Data curation (supporting); Investigation (supporting); **J. Campo:** Data curation (supporting); Investigation (equal); Writing – original draft (supporting); Writing – review & editing (supporting); **Y. Kousaka:** Data curation (lead); Funding acquisition (equal); Investigation (lead); Writing – original draft (equal); Writing – review & editing (equal); **Y. Togawa:** Data curation (equal); Funding acquisition (equal); Investigation (equal); Writing – original draft (equal); Writing – review & editing (equal).

DATA AVAILABILITY

The data that support the findings of this study are available from the corresponding author upon reasonable request.

REFERENCES

- ¹I. Dzyaloshinsky, *J. Phys. Chem. Solids* **4**, 241 (1958).
- ²T. Moriya, *Phys. Rev.* **120**, 91 (1960).
- ³T. Moriya and T. Miyadai, *Solid State Commun.* **42**, 209 (1982).
- ⁴T. Miyadai, K. Kikuchi, H. Kondo, S. Sakka, M. Arai, and Y. Ishikawa, *J. Phys. Soc. Jpn.* **52**, 1394 (1983).
- ⁵I. E. Dzyaloshinskii, *Sov. Phys. JETP* **19**, 960 (1964).
- ⁶I. E. Dzyaloshinskii, *Sov. Phys. JETP* **20**, 223 (1965).
- ⁷I. E. Dzyaloshinskii, *Sov. Phys. JETP* **20**, 665 (1965).
- ⁸Y. A. Izyumov, *Sov. Phys. Usp.* **27**, 845 (1984).
- ⁹J. Kishine, K. Inoue, and Y. Yoshida, *Prog. Theor. Phys. Suppl.* **159**, 82 (2005).
- ¹⁰Y. Togawa, T. Koyama, K. Takayanagi, S. Mori, Y. Kousaka, J. Akimitsu, S. Nishihara, K. Inoue, A. Ovchinnikov, and J. Kishine, *Phys. Rev. Lett.* **108**, 107202 (2012).
- ¹¹M. Shinozaki, S. Hoshino, Y. Masaki, J. Kishine, and Y. Kato, *J. Phys. Soc. Jpn.* **85**, 074710 (2016).
- ¹²V. Laliena, J. Campo, J. Kishine, A. S. Ovchinnikov, Y. Togawa, Y. Kousaka, and K. Inoue, *Phys. Rev. B* **93**, 134424 (2016).
- ¹³V. Laliena, J. Campo, and Y. Kousaka, *Phys. Rev. B* **94**, 094439 (2016).
- ¹⁴V. Laliena, J. Campo, and Y. Kousaka, *Phys. Rev. B* **95**, 224410 (2017).
- ¹⁵M. Shinozaki, Y. Masaki, R. Aoki, Y. Togawa, and Y. Kato, *Phys. Rev. B* **97**, 214413 (2018).
- ¹⁶Y. Masaki, R. Aoki, Y. Togawa, and Y. Kato, *Phys. Rev. B* **98**, 100402 (2018).
- ¹⁷A. N. Bogdanov and D. A. Yablonskii, *Sov. Phys. JETP* **68**, 101 (1989).
- ¹⁸A. Bogdanov and A. Hubert, *J. Magn. Magn. Mater.* **138**, 255 (1994).
- ¹⁹S. Mühlbauer, B. Binz, F. Jonietz, C. Pfleiderer, A. Rosch, A. Neubauer, R. Georgii, and P. Böni, *Science* **323**, 915 (2009).
- ²⁰X. Z. Yu, Y. Onose, N. Kanazawa, J. H. Park, J. H. Han, Y. Matsui, N. Nagaosa, and Y. Tokura, *Nature* **465**, 901 (2010).
- ²¹Y. Togawa, T. Koyama, Y. Nishimori, Y. Matsumoto, S. McVitie, D. McGrouther, R. L. Stamps, Y. Kousaka, J. Akimitsu, S. Nishihara, K. Inoue, I. G. Bostrem, V. E. Sinitsyn, A. S. Ovchinnikov, and J. Kishine, *Phys. Rev. B* **92**, 220412 (2015).
- ²²S. Tang, R. S. Fishman, S. Okamoto, J. Yi, Q. Zou, M. Fu, A.-P. Li, D. Mandrus, and Z. Gai, *Nano Lett.* **18**, 4023 (2018).
- ²³R. Aoki, Y. Kousaka, and Y. Togawa, *Phys. Rev. Lett.* **122**, 057206 (2019).
- ²⁴Y. Shimamoto, Y. Matsushima, T. Hasegawa, Y. Kousaka, I. Proskurin, J. Kishine, A. S. Ovchinnikov, F. J. T. Goncalves, and Y. Togawa, *Phys. Rev. Lett.* **128**, 247203 (2022).
- ²⁵V. Laliena and J. Campo, *Adv. Electron. Mater.* **8**, 2100782 (2022).
- ²⁶J. Kishine and A. S. Ovchinnikov, *Solid State Phys.* **66**, 1 (2015).
- ²⁷Y. Togawa, Y. Kousaka, K. Inoue, and J. Kishine, *J. Phys. Soc. Jpn.* **85**, 112001 (2016).
- ²⁸Y. Togawa, A. S. Ovchinnikov, and J. Kishine, *J. Phys. Soc. Jpn.* **92**, 081006 (2023).
- ²⁹J. M. Van Den Berg and P. Cossee, *Inorg. Chim. Acta* **2**, 143 (1968).
- ³⁰K. Anzenhofer, J. M. Van Den Berg, P. Cossee, and J. N. Helle, *J. Phys. Chem. Solids* **31**, 1057 (1970).
- ³¹B. Van Laar, H. M. Rietveld, and D. J. W. Ijdo, *J. Solid State Chem.* **3**, 154 (1971).
- ³²Y. Kousaka, T. Ogura, J. Jiang, K. Mizutani, S. Iwasaki, J. Akimitsu, and Y. Togawa, *APL Mater.* **10**, 090704 (2022).
- ³³F. Hulliger and E. Pobitschka, *J. Solid State Chem.* **1**, 117 (1970).
- ³⁴R. Friend, A. Beal, and A. Yoffe, *Philos. Mag.* **35**, 1269 (1977).
- ³⁵S. S. P. Parkin and R. H. Friend, *Philos. Mag. B* **41**, 65 (1980).
- ³⁶S. S. P. Parkin and R. H. Friend, *Philos. Mag. B* **41**, 95 (1980).
- ³⁷Y. Kousaka, Y. Nakao, J. Kishine, M. Akita, K. Inoue, and J. Akimitsu, *Nucl. Instrum. Methods Phys. Res., Sect. A* **600**, 250 (2009).
- ³⁸Y. Togawa, Y. Kousaka, S. Nishihara, K. Inoue, J. Akimitsu, A. S. Ovchinnikov, and J. Kishine, *Phys. Rev. Lett.* **111**, 197204 (2013).
- ³⁹Y. Kousaka, T. Ogura, J. Zhang, P. Miao, S. Lee, S. Torii, T. Kamiyama, J. Campo, K. Inoue, and J. Akimitsu, *J. Phys.: Conf. Ser.* **746**, 012061 (2016).
- ⁴⁰C. Zhang, J. Zhang, C. Liu, S. Zhang, Y. Yuan, P. Li, Y. Wen, Z. Jiang, B. Zhou, Y. Lei, D. Zheng, C. Song, Z. Hou, W. Mi, U. Schwingenschlögl, A. Manchon, Z. Q. Qiu, H. N. Alshareef, Y. Peng, and X. Zhang, *Adv. Mater.* **33**, 2101131 (2021).
- ⁴¹D. Obeysekera, K. Gamage, Y. Gao, S. Cheong, and J. Yang, *Adv. Electron Mater.* **7**, 2100424 (2021).
- ⁴²K. Mizutani, J. Jiang, K. Monden, Y. Shimamoto, Y. Kousaka, and Y. Togawa, "Surface barrier effect as evidence of chiral soliton lattice formation in chiral dichalcogenide CrTa₃S₆ crystals," *AIP Adv* **13**(9), 095125 (2023).
- ⁴³H. Zhang, W. Wei, G. Zheng, J. Lu, M. Wu, X. Zhu, J. Tang, W. Ning, Y. Han, L. Ling, J. Yang, W. Gao, Y. Qin, and M. Tian, *Appl. Phys. Lett.* **113**, 072402 (2018).
- ⁴⁴M. Algarni, H. Zhang, G. Zheng, J. Zhou, C. Tan, S. Albarakati, J. Partridge, E. L. H. Mayes, L. Farrar, Y. Han, M. Wu, X. Zhu, J. Tang, W. Wei, W. Gao, W. Ning, M. Tian, and L. Wang, *J. Appl. Phys.* **133**, 113902 (2023).
- ⁴⁵S. Takata, J. Suzuki, T. Shinohara, T. Oku, T. Tominaga, K. Ohishi, H. Iwase, T. Nakatani, Y. Inamura, T. Ito, K. Suzuya, K. Aizawa, M. Arai, T. Otomo, and M. Sugiyama, *JPS Conf. Proc.* **8**, 036020 (2015).
- ⁴⁶G. W. Paterson, T. Koyama, M. Shinozaki, Y. Masaki, F. J. T. Goncalves, Y. Shimamoto, T. Sogo, M. Nord, Y. Kousaka, Y. Kato, S. McVitie, and Y. Togawa, *Phys. Rev. B* **99**, 224429 (2019).
- ⁴⁷F. J. T. Goncalves, Y. Shimamoto, T. Sogo, G. W. Paterson, Y. Kousaka, and Y. Togawa, *Appl. Phys. Lett.* **116**, 012403 (2020).
- ⁴⁸L. Li, D. Song, W. Wang, F. Zheng, A. Kovács, M. Tian, R. E. Dunin-Borkowski, and H. Du, *Adv. Mater.* **35**, e2209798 (2023).
- ⁴⁹M. Ohkuma, M. Mito, H. Deguchi, Y. Kousaka, J. Ohe, J. Akimitsu, J. Kishine, and K. Inoue, *Phys. Rev. B* **106**, 104410 (2022).
- ⁵⁰M. Mito, H. Ohsumi, K. Tsuruta, Y. Kotani, T. Nakamura, Y. Togawa, M. Shinozaki, Y. Kato, J. Kishine, J. Ohe, Y. Kousaka, J. Akimitsu, and K. Inoue, *Phys. Rev. B* **97**, 024408 (2018).
- ⁵¹T. Honda, Y. Yamasaki, H. Nakao, Y. Murakami, T. Ogura, Y. Kousaka, and J. Akimitsu, *Sci. Rep.* **10**, 18596 (2020).